Applied Acoustics 203 (2023) 109193

Contents lists available at ScienceDirect

Applied Acoustics

journal homepage: www.elsevier.com/locate/apacoust

Theoretical and experimental investigations on control parameters of piezo-based vibro-acoustic modulation health monitoring of contact acoustic nonlinearity in a sandwich beam

Mohammad Ehsani [a,b], Mahnaz Shamshirsaz [a,*], Mojtaba Sadighi [b], Naserodin Sepehry [c], Richard Loendersloot [d]

[a] New Technologies Research Center (NTRC), Amirkabir University of Technology, Tehran, Iran
[b] Mechanical Engineering Department, Amirkabir University of Technology, Tehran, Iran
[c] Faculty of Mechanical and Mechatronic Engineering, Shahrood University of Technology, Shahrood, Iran
[d] Dynamics Based Maintenance, Engineering Technology, University of Twente, Enschede, Netherlands

ARTICLE INFO

Article history:
Received 4 September 2022
Received in revised form 3 December 2022
Accepted 28 December 2022

Keywords:
Contact Acoustic Nonlinearity (CAN)
Vibro-Acoustic Modulation (VAM)
Piezoelectric patch
Sensitivity Analysis (SA)
Response Surface Methodology (RSM)
Morris method
Light composite sandwich panels

ABSTRACT

Contact-type defects are prevalent in composite constructions and sandwich panels due to failure mechanisms such as bolt loosening and delamination. Contact acoustic nonlinearity is a manifestation of such defects that nonlinear health monitoring systems can detect. Vibro-acoustic modulation (VAM) is a well-established technique for the early detection of nonlinear defects in structures. It employs bi-tone excitation to reveal damage-induced nonlinearity, which results in the appearance of sidebands in the response spectrum. The objective of this research is to use PZT-based excitation to monitor bolt loosening in a sandwich beam in real-time. To address the limited capacity of the PZT transducers to excite the nonlinear mechanism, a sensitivity analysis (SA) for input factors of VAM testing was conducted to improve damage detection using the results. The Morris approach is used to investigate the sensitivity of VAM damage metrics derived analytically in the frequency domain. To reduce the number of tests required for the experimental SA, the response surface methodology (RSM) is applied. The analysis of variance and Fischer's statistics are used to calculate the SA of experimental damage indices. In RSM computations, the discrete influence of excitation frequencies on the modulation sidebands is addressed. For reliable SA of experimental results, the effect of background noise is taken into account. The findings of this study may be applied to the selection of appropriate damage metrics in real-world applications of VAM health monitoring systems, as well as the effective tuning of input control parameters to maximize damage detectability.

1. Introduction

Sandwich constructions are gaining popularity in the aerospace, automotive, and marine industries due to their relative benefits over other structural materials in terms of weight, bending stiffness, stability, and energy absorption [1]. In typical sandwich panels, two stiff metallic or composite thin face sheets are separated by open or closed-cell foam or a honeycomb-like thick core of low density. Sandwich architectures are commonly employed in applications where durability and damage tolerance are primary considerations. The requirement for online/on-demand monitoring of metallic and composite structures has prompted the development of structural health monitoring (SHM) based on permanently installed or integrated piezoelectric transducers [2,3]. Through conditional-based maintenance, SHM increases the reliability and availability of the monitored structures while lowering maintenance costs.

Contact-type defects in composite constructions and sandwich panels include loose bolted joints [4–10], breathing cracks due to core crushing or fiber/matrix cracking [11–13], delamination [14–17], and debonding between the core and skins [18]. Some nonlinear mechanisms that can occur at the contact interface include asymmetric stiffness due to the opening and closing of cleanly separated cracks or changes in the contact pressure of closed cracks [16], stress–strain hysteresis [19], amplitude-dependent dissipation [20], and thermoelastic coupling [19]. The most common classification for these mechanisms is non-classical nonlinearities, which are local and operate on various length scales [14]. Non-classical nonlinear manifestations include

* Corresponding author.
E-mail address: shamshir@aut.ac.ir (M. Shamshirsaz).

https://doi.org/10.1016/j.apacoust.2022.109193
0003-682X/

higher or sub-harmonic generation [21], slow dynamics [22], cross-modulation [23], and intermodulation [24]. Several nonlinear health monitoring methods based on nonlinear mechanisms generated by flaws have emerged for early damage detection. Vibro-acoustic modulation (VAM), which is based on the intermodulation concept, has received interest among other techniques due to its ease of implementation, proper sensitivity to incipient damage [25,26], and reduced influence from non-damage-related nonlinearities [27].

In VAM, the monitored structure is interrogated using a combination of a low-frequency, large-amplitude pumping vibration and a high-frequency, low-amplitude carrier (also known as a probe) wave [24]. Pump excitation activates the nonlinear mechanism by pumping energy into the structure. The function of the carrier signal is to probe for damage and then carry damage-related data to the sensor. The structural response is primarily linear in the intact or undamaged state, with only the fundamental input harmonics overlaid in the response spectrum. In the damaged state, the interaction of excitation waves with the damage generates superharmonics and intermodulation of the input harmonics in addition to the input frequencies. Sidebands are intermodulation frequencies that emerge at a multiple of the pump frequency (f_p) around the carrier frequency (f_c) component or its superharmonics, i.e., $mf_p \pm nf_c$ ($m, n = 1, 2, \ldots$). The presence of sideband components confirms the presence of a defect, which is the basic premise behind VAM-based damage detection. Damage indices (DI) are used to quantify damage by processing the sensed signal in the time [28], frequency [7,12,29], or time–frequency domains [21,30,31]. The Hilbert transform (HT), which belongs to the latter group, is a common signal processing tool for demodulating the received signal and extracting amplitude and phase modulation DIs [8,32,33]. According to some studies, demodulating the sensory signal in VAM can reveal small sidebands buried beneath the background noise or carrier frequency sidelobes in the case of very low-frequency pump actuation [34], as well as provide information on the type of damage [30,35], or damage growth stage [36].

The appropriate selection of input adjustable parameters, including voltage amplitudes and frequency of the pump and carrier signals, is critical to the successful implementation of VAM testing [9,37,38]. Optimal input settings result in proper nonlinear mechanism activation in the defective zone, higher DI, and improved damage detection [7,16]. The carrier frequency (f_c) is frequently set in the ultrasonic range and is matched with a local mode of vibration unique to the defect shape known as local defect resonance (LDR) [38,39]. The LDR is determined using data on vibration mode shapes, which can be obtained numerically or experimentally [14,40]. The pump frequency (f_p) is typically chosen in the acoustic range, usually matching one of the structure's first few modal frequencies as determined by a modal analysis [41]. Regarding the amplitude of the pump and carrier excitations, increasing the input voltages increases the amount of energy injected into the defective area and the relative motion at the contact interface. However, increasing the voltage causes some undesirable nonlinear effects [12,24], including disordered modulation induced by the nonlinearity of the boundary and medium [2]. As a result, using a baseline signal [12] or separating damage-induced nonlinearities from measurement system nonlinearities is necessary [42]. High-voltage risks also diminish the safety level of the monitored system. Meanwhile, lowering the excitation voltage may make the modulation effect insensitive to damage or invisible in noisy environments [2], especially when low-profile PZT patches are used in the driving chain rather than electromagnetic shakers [7], PZT stacks [33], or permanent magnets [43]. This all implies the trade-off nature of amplifying voltages in VAM tests and calls for an optimization task to find their appropriate value [44].

The switch to nonlinear approaches such as VAM for health monitoring is primarily motivated by the need to improve the sensitivity of damage detection [45]. They are commonly used to detect incipient damage at the onset and evolution stages. Minor subtle damage sidebands have small amplitudes and can be hidden in noise components, making them undetectable [46]. Environmental noise has a major influence on detection probability [9]. Therefore, noise analysis is necessary for damage identification problems based on VAM. Lim et al. [47] estimated the noise threshold by averaging the response to carrier actuation alone at the modulation frequencies. The threshold was considered while calculating the nonlinearity indices, and their probability distributions were then used to develop a robust damage classifier. Because PZT transducers have a limited capacity to pump energy to the defective area, spectral sidebands are more likely to be buried in the background noise. To estimate the background noise level from the remaining signal, notch filters are used in this study to remove peaks larger than a predefined threshold. The measured noise level is supplemented with a safety factor to calculate reliable damage indices.

The purpose of this study is to improve damage detection in VAM health monitoring by developing an optimization framework for selecting appropriate input control parameters. The response surface method (RSM) is used to design the minimum number of experiments necessary to cover the design space up to the second order. RSM calculations take into account the discrete character of the frequency response function, which results in a discontinuous influence of excitation frequencies on the DIs. A sensitivity analysis (SA) of some spectral and demodulation-derived DIs for VAM input control parameters is performed to illustrate their relationship, and input parameters are ranked in terms of importance for damage detectability. A similar procedure is provided when a physical model of VAM is available. In this regard, the analytical expression of intended DIs in terms of input control parameters is determined using a simple single degree of freedom (SDOF) model. The pin force model is used to link the mechanical model to the electromechanical effects of the actuator and sensor PZTs. Instead of RSM, sample-based SA is used, which can deal with more complex input–output relationships. The Morris and Sobol' approaches are used in the theoretical SA, with the former being more suited to models with high computational costs and the latter for validating the former results. Theoretical and experimental SA results are also compared. Finally, some guidelines for choosing an appropriate DI for damage identification and tuning input parameters to maximize damage detectability depending on the selected DI are offered.

2. Physical theory of contact-induced vibro-acoustic modulation

The transmission and reflection of waves over a damaged contact interface cause nonlinear characteristics [48]. Contact conditions, such as contact pressure, topography, and material properties of the mating surfaces, influence how waves interact with the contact interface [49]. When the wavelength of the diagnostic waves is longer than the typical length scale of surface topography, the dynamic response is dominated by static contact characteristics, and the macroscopic interfacial stiffness can be approximated by springs of equivalent stiffness [50]. A simplified representation of the dynamic contact of the sandwich beam with the loose bolt is illustrated in Fig. 1. The rough interface contact force can be approximated as a power function of the gap distance g between the contact surfaces [48,51]:

$$F(g) = Cg^n, \; C > 0, \; n > 1 \tag{1}$$

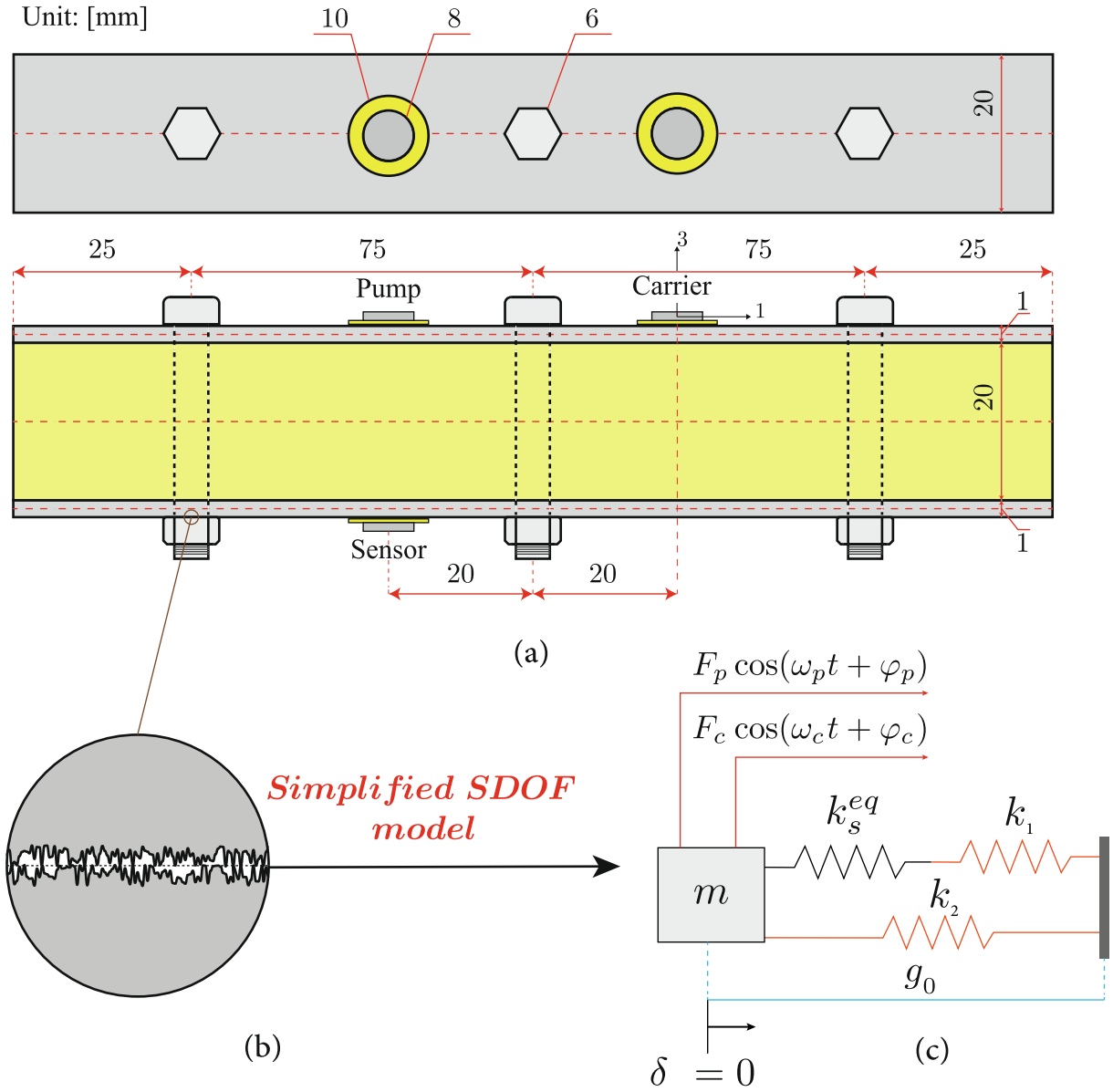

Fig. 1. Schematic of the test specimen, transducers, and bolted joints along with the simplified model of the contact dynamics at the interface of the sandwich beam with a loose bolt; the polarization direction of the PZTs is illustrated on the carrier transducer.

The value of n varies depending on the topography of the mating surface and is typically between 1.17 and 2.11 [51]. In the absence of the mixed excitation, the contact pair is in equilibrium under the nominal force F_0 at the equilibrium gap distance g_0. In this case, the bolt force can be related to the applied torque T as follows [52]:

$$F_0 = Cg_0^n = \frac{T}{Kd} \tag{2}$$

where K is the torque coefficient and d is the bolt nominal diameter. By introducing the mixed excitation of VAM, the gap distance, and therefore the contact pressure and force, are varied periodically. As a result, the structure is subjected to a periodic force F_{CAN}, which can be expressed as follows using Eq. (1) and Eq. (2):

$$F_{CAN} = C(g_0+\delta(t))^n - F_0 = C(g_0+\delta(t))^n - Cg_0^n \tag{3}$$

where $\delta(t)$ denotes the variation in gap distance from the equilibrium state g_0 over time t. Using the Taylor series to expand the dynamic part of the contact force F_{CAN} up to the second order, we get:

$$F_{CAN} = C\left(g_0^n + ng_0^{n-1}\delta(t) + \frac{n(n-1)}{2}g_0^{n-2}\delta^2(t) + \mathcal{O}(\delta^3(t)) - g_0^n\right) \tag{4}$$

where $\mathcal{O}(\delta^3(t))$ contains terms of a greater order than 3 in respect of $\delta(t)$. F_{CAN} can be expressed in the following way using equivalent stiffnesses:

$$F_{CAN} = k_1\delta(t) + k_2\delta^2(t) + \mathcal{O}(\delta^3(t)) \tag{5}$$

where k_i (i = 1, 2) is defined as follows:

$$k_i = \binom{n}{i}Cg_0^{n-i} = \binom{n}{i}C^{\frac{i}{n}}(F_0)^{\frac{n-i}{n}} = \binom{n}{i}C^{\frac{i}{n}}\left(\frac{T}{Kd}\right)^{\frac{n-i}{n}} \tag{6}$$

where $\binom{n}{i}$ indicates the binomial coefficient (see the **supplementary file** for noninteger exponent binomial theorem). Eq. (2) has been utilized to connect the contact stiffness to the bolt torque in the above formula. The configuration of the equivalent springs

for contact force and their relationship to the equivalent stiffness of the structure at the contact position is illustrated in Fig. 1 (c). The equivalent bulk stiffness k_s^{eq} is in series with the linear contact stiffness k_1 [51], while their set is in parallel with the nonlinear contact stiffness. Thus, the equivalent linear stiffness at the point of contact (k_l) can be calculated as follows:

$$k_l = \frac{k_1 k_s^{eq}}{k_1 + k_s^{eq}} \overset{k_1 \gg k_s^{eq}}{\simeq} k_s^{eq} \tag{7}$$

In the approximation of the aforementioned equation, the fact that the first-order contact stiffness value k_1 (in the order of 1×10^{15} [48]) is much greater than the equivalent bulk stiffness k_s^{eq} is used.

Under mixed excitation, the equation of motion of an SDOF system in contact with a rough surface is expressed as:

$$m\ddot{\delta}(t) + k_l\delta(t) + \varepsilon k_2\delta^2(t) = F_p\cos\left(\omega_p t + \varphi_p\right) + F_c\cos\left(\omega_c t + \varphi_c\right) \tag{8}$$

where ε is the perturbation parameter that scales the nonlinear effect to be orders of magnitude less than the linear response and reflects the local nature of the contact nonlinearity, F_p (F_c), ω_p (ω_c) and φ_p(φ_c) are the amplitude, frequency and phase of the pump (carrier) excitation force, respectively, and m is the equivalent mass at the contact zone. Higher-order contact stiffness related to $\mathcal{O}(\delta^3(t))$ is disregarded in the equation of motion (Eq. (8)). F_p and F_c may be linked to the PZT excitation voltage through ideal shear lag analysis [53]:

$$F_a \simeq \eta\frac{k_s h_s}{\kappa k_{pzt}h_{pzt} + k_s h_s}k_{pzt}h_{pzt}\left(-d_{31}\frac{V_a}{h_{pzt}}\right) \tag{9}$$

where k_{pzt} and h_{pzt} are the PZT stiffness and thickness, k_s and h_s are the structural stiffness and thickness, d_{31} is the piezoelectric constant, and V_a is the applied voltage. The subscript a in the above equation is a dummy, and it can be either p or c, which refers to pump or carrier actuation. The coefficient κ in Eq. (9) is determined by the mode shapes across the beam thickness and η denotes the proportion of excitation forces at the contact point. Dividing Eq. (8) by m simplifies it to the following form:

$$\ddot{\delta}(t) + \omega_0^2\delta(t) = -\varepsilon\frac{k_2}{m}\delta^2(t) + A_p\cos\left(\omega_p t + \varphi_p\right) + A_c\cos\left(\omega_c t + \varphi_c\right) \tag{10}$$

where ω_0 is the natural frequency at the contact zone defined as $\sqrt{k_l/m} \simeq \sqrt{k_s^{eq}/m}$ according to Eq. (7), and $A_p = F_p/m$, $A_c = F_c/m$ are proportional to the amplitudes of the excitation accelerations. The steady-state response of Eq. (10) with zero initial conditions $\delta(0) = \dot{\delta}(0) = 0$ is as follows according to the perturbation theory [7,32]:

$$\begin{aligned}\delta(t) = {} & H_p\cos\left(\omega_p t + \theta_p\right) + H_c\cos\left(\omega_c t + \theta_c\right) + G_{dc} + G_{hp}\cos\left(2\omega_p t + \theta_{hp}\right) + \\ & G_{hc}\cos\left(2\omega_c t + \theta_{hc}\right) + G_{sb^-}\cos\left(\left(\omega_c - \omega_p\right)t + \theta_{sb^-}\right) + G_{sb^+}\cos\left(\left(\omega_c + \omega_p\right)t + \theta_{sb^+}\right)\end{aligned} \tag{11}$$

Assuming zero-phase actuation signals ($\varphi_p = \varphi_c = 0$) results in zero phases for the sensor signal components in the considered CAN model. The expressions for the amplitude of the harmonics $H_p, H_c, G_{hp}, G_{hc}, G_{sb^-}, G_{sb^+}$ are listed in **Appendix A**.

To extract the spectral DIs, the Fourier transform is applied to the solution in Eq. (11). According to the form of the solution, the coefficients of the harmonics are equal to the amplitude of the peaks in the frequency domain. The DI_1 is defined as the sum of the amplitudes of the first pair of sidebands around ω_c as follows:

$$\begin{aligned}DI_1 &= G_{sb^-} + G_{sb^+} \\ &= \frac{2\varepsilon k_2 A_c A_p\left(\omega_c^2 + \omega_p^2 - \omega_0^2\right)}{m\left(\omega_0^2 - \omega_c^2\right)\left(\omega_0^2 - \omega_p^2\right)\left(\omega_0^4 - 2\omega_0^2\left(\omega_c^2 + \omega_p^2\right) + \left(\omega_c^2 - \omega_p^2\right)^2\right)}\end{aligned} \tag{12}$$

DI_1 is suitable for damage imaging [19,20]. The DI_2 is defined as the normalized counterpart of the DI_1 with H_pH_c [6]:

$$\begin{aligned}DI_2 &= \frac{G_{sb^-} + G_{sb^+}}{H_pH_c} \\ &= \frac{2\varepsilon k_2\left(\omega_c^2 + \omega_p^2 - \omega_0^2\right)}{m\left(\omega_0^4 - 2\omega_0^2\left(\omega_c^2 + \omega_p^2\right) + \left(\omega_c^2 - \omega_p^2\right)^2\right)}\end{aligned} \tag{13}$$

Normalization by H_p [16], H_c [7,19], $H_p + H_c$ and $\sqrt{H_pH_c}$ [15] has also been used in previous studies, and comparable analytical expressions can be derived for those cases as well.

The Hilbert transform is used to separate the amplitude and phase modulation of the response in Eq (11). A band-pass filter with a passband of $f_c \pm nf_p$ (n = 1) is applied to retain only the carrier and sideband components, bringing the response closer to the monoharmonic signal that is best suited for HT analysis. The analytical signal $\delta_a(t)$ is obtained as follows:

$$\begin{aligned}\delta_a(t) &= \delta_{bp}(t) + i\hat{\delta}_{bp}(t) \\ &= e^{i(\omega_c t + \theta_c)}\left(H_c + G_{sb^-}e^{-i\left(\omega_p t + \theta_c - \theta_1\right)} + G_{sb^+}e^{i\left(\omega_p t - \theta_c + \theta_2\right)}\right)\end{aligned} \tag{14}$$

where $\delta_{bp}(t)$ is the band-passed response around the carrier frequency, $\hat{\delta}_{bp}(t)$ represents its Hilbert transform, and i represents the imaginary unit. The instantaneous amplitude $A_{ins}(t)$ and phase $\varphi_{ins}(t)$ are extracted using the moduli and angle of the above complex signal. The following AM and FM depth definitions are used as demodulation DIs:

$$DI_3 = A_{ins_{pp}}/2H_c \tag{15}$$

$$DI_4 = \omega_{ins_{pp}}/2\omega_p = \max|\omega_{ins} - \omega_c|/\omega_p \tag{16}$$

The PP subscripts represent the peak-to-peak values of instantaneous characteristics. By inserting A_{ins} and ω_{ins} from Eq. (14) and assuming zero phases for the sensor signal spectral components, demodulation DIs are derived as follows:

$$DI_3 = \frac{2\varepsilon k_2 A_p\left(\omega_c^2 + \omega_p^2 - \omega_0^2\right)}{m\left(\omega_0^2 - \omega_p^2\right)\left(\omega_0^4 - 2\omega_0^2\left(\omega_c^2 + \omega_p^2\right) + \left(\omega_c^2 - \omega_p^2\right)^2\right)} \tag{17}$$

$$DI_4 = \frac{4\varepsilon k_2 A_p\omega_c\omega_p}{2\varepsilon k_2 A_p\left(\omega_c^2 + \omega_p^2 - \omega_0^2\right) + m\left(\omega_0^2 - \omega_p^2\right)\left(\omega_0^4 - 2\omega_0^2\left(\omega_c^2 + \omega_p^2\right) + \left(\omega_c^2 - \omega_p^2\right)^2\right)} \tag{18}$$

The derivation of DI_3 and DI_4 is detailed in **Appendix B**.

3. Sensitivity analysis

3.1. ANOVA-based experimental sensitivity analysis

The frequency response of the system determines how excitation frequencies affect modulation intensity [54]. Sidebands are only visible in practice when the actuation frequencies are close to natural frequencies, or LDR [18,40]. Fading of the sidebands occurs when the actuation frequencies are moved away from their optimal values. As a result, excitation frequencies have a discrete effect on modulation indices. To account for the discontinuous nature of excitation frequencies, the response surface method (RSM)

with both continuous and discrete independent variables is used as follows:

$$y = \beta_0 + \sum_{i=1}^{m}\beta_i x_i + \sum_{i=1}^{m}\beta_{ii}x_i^2 + \sum_{j=1i<j}^{m}\sum_{i=1}^{m}\beta_{ij}x_i x_j + \sum_{j=2}^{d}\sum_{i=1}^{p}\gamma_{ij}D_{ij} + \sum_{l=2}^{d}\sum_{k=1\,i<k}^{p}\sum_{j=2}^{d}\sum_{i=1}^{p}\lambda_{ijkl}D_{ij}D_{kl} + \sum_{k=2}^{d}\sum_{j=1}^{p}\sum_{i=1}^{m}\mu_{ijk}x_i D_{jk} + \epsilon \quad (19)$$

where y is the response (target DI), x_i the i^{th} independent continuous variable, m the number of continuous variables, D_{ij} is a dummy variable for the i^{th} independent categorical variable (D_i) at the j^{th} level (d_j), p is the number of categorical variables, d the number of levels for each categorical variable, and ϵ the random effect of experimental error. β_0, β_i, β_{ii}, β_{ij}, γ_{ij}, λ_{ijkl}, μ_{ijk} are the regression coefficients. The level of categorical variables is determined by dummy variables, which are defined as follows:

$$D_{ij} = \begin{cases} 1 & D_i = d_j \\ 0 & D_i \neq d_j \end{cases} \quad (20)$$

If the i^{th} categorical variable (D_i) is on the j^{th} level (d_j), the dummy variable D_{ij} equals 1; otherwise, it equals 0. Each categorical variable with d levels requires the use of $d-1$ dummy variables, one of which serves as the reference level [55]. RSM can rank the relative relevance of control inputs on system performance.

3.1.1. Design space

Pump voltage (V_p), carrier voltage (V_c), pump frequency (f_p), and carrier frequency (f_c) make up the four-dimensional design space that contains the four control settings of VAM testing. The central composite design (CCD) is used to design the experiments. Table 1 shows the range of excitation voltages that are considered continuous variables. The values of excitation frequencies are calculated using a combination of transfer impedance (TI) [56] and LDR analysis, as will be discussed in Section 4.1.$2^2 + 2 \times 2 + 1 = 9$ experiments are required for two continuous variables with one replication at the center point in CCD. There are $3 \times 3 = 9$ permutations for the two categorical variables, each with three levels, bringing the total number of required runs to $9 \times 9 = 81$. Each experiment was repeated ten times to reduce estimation variance, and the results were averaged. To estimate the coefficients using the ordinary least squares approach, the acquired data is introduced to Eq. (19) [57].

3.2. Theoretical sensitivity analysis using the Morris method

The Morris approach, which is a sample-based method with a low computing cost, was utilized for theoretical SA. The Morris method is an iterative and randomized version of the one-factor-at-a-time design, which is an efficient and reliable screening methodology [58]. It can calculate global sensitivity measures using so-called elementary effects (EE), which are defined as the ratio of output variation in response to a perturbation of the i^{th} input factor (X_i) as follows:

$$EE_i(\mathbf{x}) = \frac{\mathscr{M}(x_1,\ldots,x_i+\Delta,\ldots,x_M) - \mathscr{M}(\mathbf{x})}{\Delta};\ \mathbf{x} \in \mathscr{G} \quad (21)$$

where EE_i is the elementary effect of the i^{th} control variable calculated at the point $\mathbf{x}$ from a gridded input space $\mathscr{G}$, and $\mathscr{M}$ is the computational model associated with each derived DI. The trajectory-based sampling approach was utilized to design r trajectories for calculating the EEs [59]. The Morris method's sensitivity indices are moments estimators of the EEs' finite distribution $\boldsymbol{F}_i$ computed over r trajectories:

$$\hat{\mu}_i = \frac{1}{r}\sum_{j=1}^{r} EE_i^{(j)};\ \hat{\mu}_i^* = \frac{1}{r}\sum_{j=1}^{r}\left|EE_i^{(j)}\right| \quad (22)$$

$$\hat{\sigma}_i = \sqrt{\frac{1}{r-1}\sum_{j=1}^{r}\left(EE_i^{(j)} - \hat{\mu}_i\right)^2} \quad (23)$$

where $\hat{\mu}_i$ is the mean and $\hat{\sigma}_i$ is the standard deviation of the $\boldsymbol{F}_i$. $\hat{\mu}_i^*$ is based on the absolute value of the EEs to address the canceling out effects that may be contained in $\hat{\mu}_i$ [58,59]. The likelihood of a nonlinear or interactive influence of the control parameter on the response grows when the coefficient of variation $CoV_i = \sigma_i/\mu_i^*$ is increased. If the EEs have a normal distribution, CoV_i can be used to determine the type of effect, such as linear, nonlinear, monotonic, or nonmonotonic [60].

3.2.1. Design space and parameters of the physical model

The target DIs, i.e., Eqs. (12), (13), (17), and (18) are served as the computational functions $\mathscr{M}(\mathbf{X})$ for determining the EEs. The pump and carrier voltages and frequencies are the inputs to DI's functions, i.e., $\mathbf{X} = \{V_p, V_c, f_p, f_c\}^T$. Table 2 shows the range of input variables. The chosen ranges conform with the experimental values; see also Table 1. The frequency range considered for the pump actuation corresponds to the frequency range of TI tests used to determine the levels given in Table 1, see Section 4.1. The carrier actuation range was limited to the low and high levels employed in the experiments since it is wide enough to explore its influence on DIs. The natural frequency ($f_0 = \omega_0/2\pi$) at the contact point is 111250 Hz, which is sufficiently far away from the pump and carrier frequencies. The pump and carrier frequencies can be sampled continuously as long as there are no natural frequencies within the specified range.

The input voltages are converted to the actuation forces using Eq. (9). The values used for quantities within the pin force model

Table 2
Control parameters of VAM tests and their ranges that are used in the sensitivity analysis of analytical DIs.

Variable	Notation	Lower bound	Upper bound	Units
Pump voltage	V_p	50	160	[V]
Carrier voltage	V_c	10	40	[V]
Pump frequency	f_p	100	1000	[Hz]
Carrier frequency	f_c	190,000	222,000	[Hz]

Table 1
Design space, type, and levels of the input control variables for the experimental sensitivity analysis of DIs.

			Levels			
Factor	Notation	Type	Low (-1)	Intermediate (0)	High (+1)	Units
Pump voltage	V_p	Continuous	50	100	160	[V]
Carrier voltage	V_c	Continuous	10	25	40	[V]
Pump frequency	f_p	Categorical	155	255	475	[Hz]
Carrier frequency	f_c	Categorical	190,000	206,000	222,000	[Hz]

Table 3
Geometrical and material parameters of the structure and PZT used within the pin force model.

k_s[GPa]	k_{pzt}[GPa]	h_s[mm]	h_{pzt}[mm]	d_{31}[m/V]
70	62	22	0.5	-320×10^{-12}

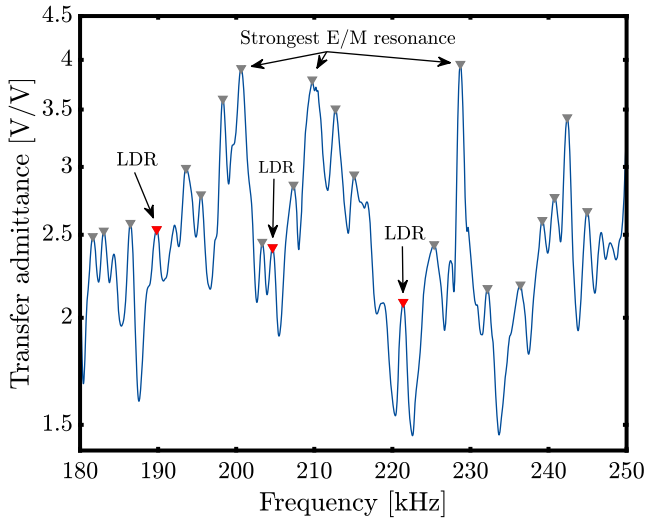

Fig. 2. Admittance spectrum for the carrier actuation in the 180–250 kHz range; the gray-marked peaks indicate candidate frequencies for VAM tests, while the red-marked peaks are selected LDR peaks. (For interpretation of the references to colour in this figure, the reader is referred to the web version of this article.)

of Eq. (9) are given in Table 3. The value of η was set to 1×10^{-6}, which represents a micro-scale interaction. The coefficient κ was taken as 4 in computations [53]. A_p and A_c in DI expressions are calculated by dividing the actuation forces obtained using Eq. (1) by the effective mass at the contact point m. m was calculated to be 2.14×10^{-11}. The values of C and n in Eq. (6) were chosen to be 8×10^{15} and 3/2, where the latter is in accordance with Hertzian contact. F_0 was considered 10^7 [48]. ε was set to the k_1/k_2 ratio, i.e., 4.64×10^{-6}.

3.2.2. Convergence analysis and validation of Morris sensitivity measures

The Morris sensitivity measures were subjected to convergence studies to determine the optimal number of replications (r) and sampling density (p). A convergence study was carried out by simultaneously raising r and p and monitoring the relative change in the sensitivity measures. The findings show that a sampling density of 6 resulted in proper gridding of the input space and fast convergence of the sensitivity measures. To ensure the Morris sensitivity measure is converged to validated results, the outcomes are compared with the Sobol' SA results with 60,000 samples. To compare the sensitivity indices quantitatively, the outcomes for both methods are scaled between 0 and 1. The adjusted sensitivity indices are compared graphically in Fig. 9. The results demonstrate conformity between Morris and Sobol's results for all DIs. The rank of control parameters in terms of importance is also the same in both methods for all DIs.

4. Test specimen and experimental setup

A sandwich beam with aluminum face sheets and a polyurethane core with three bolted joints serves as the test sample. Fig. 1 illustrates the sandwich beam and the bolts' dimensions. Two actuators and one sensing piezoelectric disc were installed

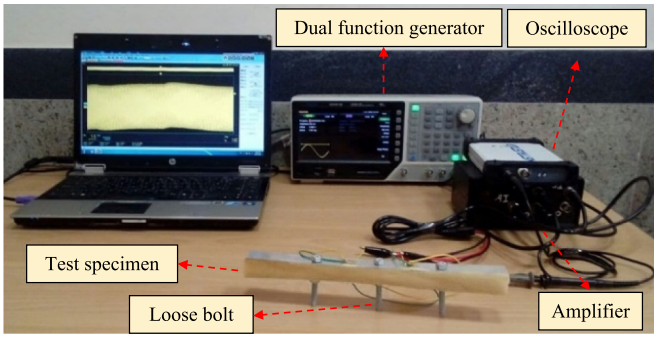

Fig. 3. VAM test setup; The test specimen geometry and sensor placements are illustrated in Fig. 1.

on the beam, each with a diameter of 10 mm. Two-part epoxy is used to permanently bind the PZT patches to the beam. Fig. 1 depicts the position of the piezoelectric sensors.

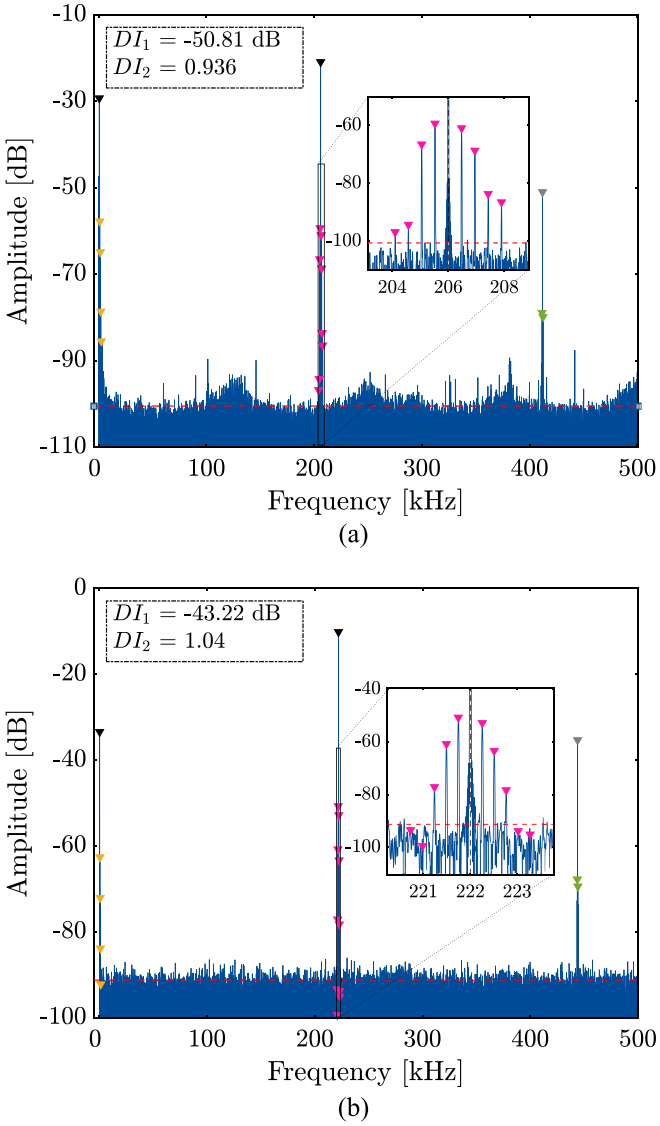

Fig. 4. The response spectra of two VAM experiments in the case of a loose bolt; control parameters: (a) V_p = 160 V, V_c = 25 V, f_p = 475 Hz, f_c = 206 kHz; (b) V_p = 100 V, V_c = 40 V, f_p = 255 Hz, f_c = 222 kHz; The inset shows the magnified spectrum around the carrier frequency.

4.1. Determination of pump and carrier frequencies using transfer impedance tests

To improve sensor signal strength and eliminate vibrational standing points, VAM tests' excitation frequencies are chosen as the sensor patch's Electro-Mechanical (E/M) resonances. The pitch-catch scheme is used to transmit diagnostic waves in VAM tests. The E/M modes can also be determined in a similar manner using TI measurements [61]. In TI tests, the actuator patch emits a broadband frequency sweep as a chirp signal. The actuation signal was generated by the HDG2002B. By dividing the sensor voltage spectrum by the actuation voltage spectrum, the E/M

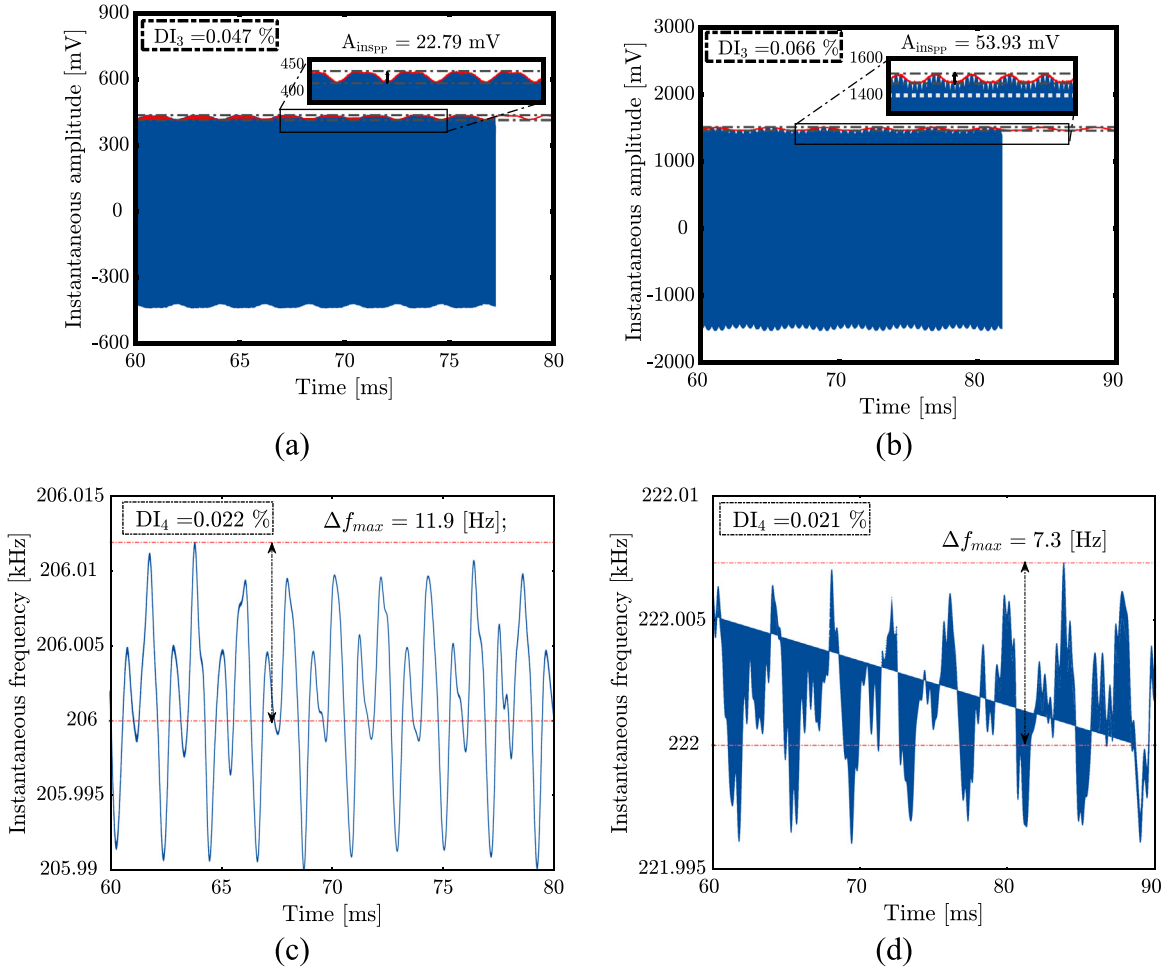

Fig. 5. Extraction of demodulation DIs using HT analysis; (a), (b) bandpass filtered signals with envelopes (instantaneous amplitude) and peak-to-peak value as DI_3; (c), (d) instantaneous frequency and peak-to-peak value as DI_4; the raw signal of the left and right figures corresponds to signals (a) and (b) of Fig. 4.

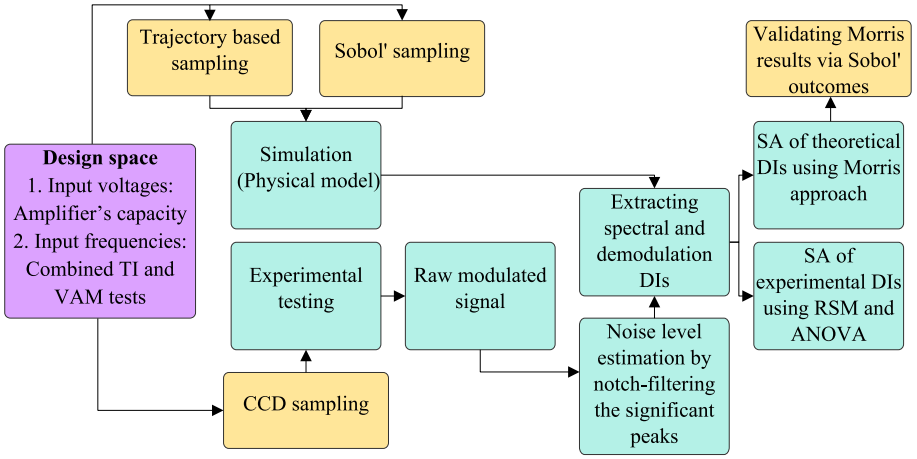

Fig. 6. The procedure of theoretical and experimental SA of the VAM-derived DIs for control parameters.

admittance spectrum is calculated. The pump-sensor and carrier-sensor patch pathways are used for the TI test, with frequencies ranging from 10 to 1000 Hz for the former and 180 to 250 kHz for the latter. The admittance spectrum's peak frequencies are appropriate candidates for excitation frequencies [15,62]. The frequency of pump actuation is set at the highest peaks of the admittance spectrum, which corresponds to the strongest E/M resonance. To find LDRs, VAM experiments are carried out on all conceivable combinations of peak frequencies in the carrier range (Fig. 2) with the selected pump frequency. The carrier frequencies were chosen based on which frequency combinations produced the greatest sidebands. It is worth noting that the LDR frequencies correspond to the local mode shapes of damage and do not necessarily coincide with the highest peaks in the spectrum [14].

4.2. VAM tests

Two synchronously applied continuous sinusoidal waves serve as excitation signals for VAM tests. The HDG2002B two-channel waveform generator transmits sinusoidal signals to actuator patches. The amplifier increases the amplitude of the waves. The excitation signals' amplitude and frequency are adjusted in line with the experimental design given in Table 1. The sensor patch is attached to an oscilloscope (ISDS206a) with a sampling rate of 25 MS/s to measure the modulated wave. To obtain a high-resolution response spectrum, the sensor data is captured for 0.5 s of steady-state vibrations. To improve the signal-to-noise ratio, each test was repeated 10 times and the results were averaged in the frequency domain (amplitude averaging [24]). The experimental setup is depicted in Fig. 3.

The fully tightened (15 N.m torque) and loose bolts correspond to the structure's intact and defective states. To ensure that the emerging sidebands in the defective case are not related to intrinsic or measurement chain nonlinearities, the intact condition tests were carried out for multiple combinations of input frequencies with both stimulations at their maximum amplitude levels. By loosening the middle bolt to 2 N.m of torque, the defect is introduced. In all VAM tests, the level of bolt loosening and, as a result, the defect intensity are the same.

4.3. Processing of the modulated signal and target DI extraction

The damage indices were calculated by processing modulated signals obtained from the experimental testing. In the time domain, signal processing comprises eliminating major frequency components from the response using the notch (band-stop) filter and estimating the noise level of the remaining signal. Linear, superharmonic, and modulation components, as well as some other environmental or measurement chain-driven harmonics such as powerline frequency, are among the removed peaks. The noise level in the time and frequency domains is measured by averaging throughout the residual notch-filtered signal.

Frequency domain analysis entails identifying sidebands in the response spectrum and computing damage metrics while accounting for noise effects. The signal's spectrum is estimated using a fast Fourier transform with a Blackman window, the latter for reducing the sidelobes. The spectral DIs are defined in the same way as in the analytical case (Eq. (12) and Eq. (13)), except the frequency noise level is subtracted from the spectral amplitudes. The spectral DIs' values are annotated in Fig. 4 for two cases of experimental tests.

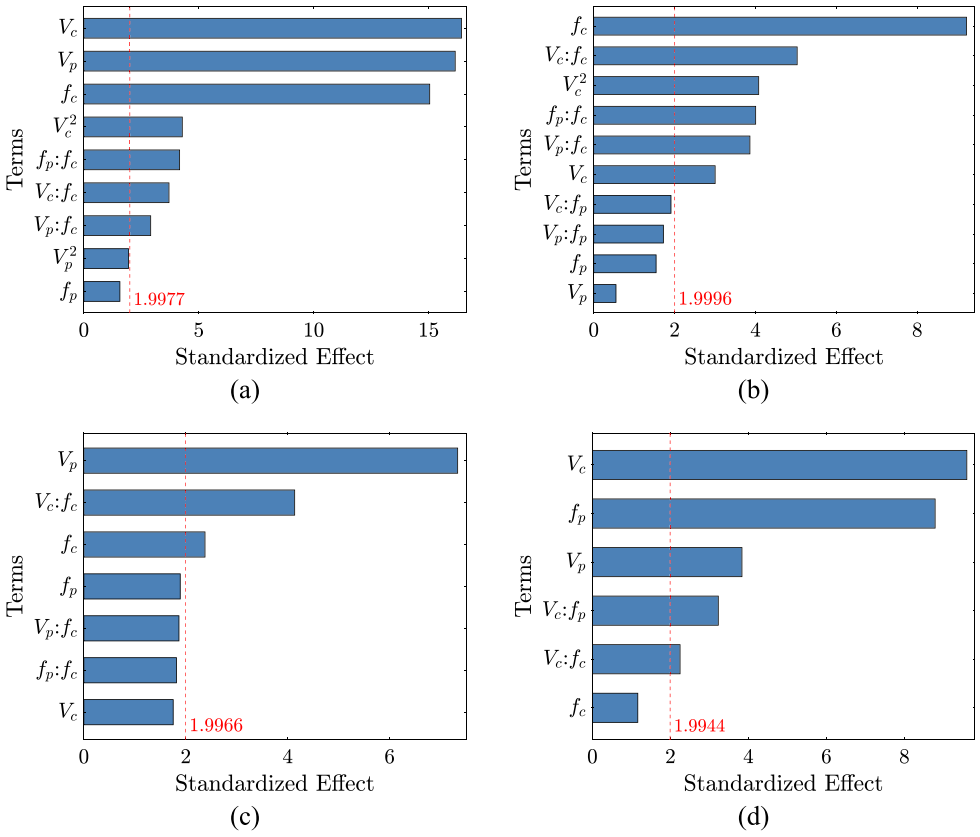

Fig. 7. Standardized effects of control parameters on the damage indices in the form of Pareto plots; (a) DI_1; (b) DI_2; (c) DI_3; (d) DI_4; (vertical line corresponds to a significance level of 0.05).

Signal demodulation in the time–frequency domain is performed in the same manner as in Section 2. The modulated signal is first filtered with a passband of $2nf_p$ around the carrier frequency, where n was assumed to be 1. The Hilbert transform was applied to the filtered signal, and the analytical signal was computed. The analytical signal was used to calculate the instantaneous amplitude and frequency; see Fig. 5. DI_3 and DI_4 are obtained by substituting the peak-to-peak values of the instantaneous features in Eq. (15) and Eq. (16).

To summarize, each experiment provided four DIs after processing the raw signal. The computed DIs are stored in a set $\boldsymbol{y} = \{DI_1, \ldots, DI_4\}$ to form the quantities of interest in the RSM process. Fig. 6 shows the steps for identifying the design space, sampling the design space, running experiments, processing the modulated signal, and performing SA.

5. Results and discussion

The SA findings of analytical and experimental DIs for VAM control settings are presented in this section. Individual effects of control settings on the target DI are examined to exclude interaction effects from SA results, which are primarily caused by non-damage-related nonlinearities. The correlation between the target DI and control parameters is also investigated to further explore the tuning procedure that results in improved damage detection.

5.1. Sensitivity of the target DIs for control parameters

Fig. 7 shows the SA results of experimental DIs using the square root of the F-statistic. The vertical lines in the figures represent the 95 % confidence level. Factors with a standardized effect smaller than the significance level are statistically unimportant and may be disregarded.

Fig. 8 shows the convergent Morris SA results, i.e., with 100 replications and a resolution of 6, for the target DIs. The total number of simulations used to derive the data in Fig. 8 is 500. In each case, the confidence intervals for the estimation of the mean and standard deviation of Eq. (22) and Eq. (23) are plotted for the 95 % confidence level. The $\sigma - \mu^*$ planes in Fig. 8 are delimited by the CoV criterion [60,63].

To compare the theoretical and experimental SA results, the outputs are scaled between 0 and 1. For the experimental outcomes, the overall effect of every control variable is calculated by adding its individual and interaction effects. Fig. 9 compares the normalized version of the total standardized effects of RSM analysis, Morris measures μ^*, and total Sobol indices S^T for all DIs.

According to the results, the V_c, V_p, and f_c parameters have the largest influence on the DI_1, whereas the f_p factor has minimal effect. When it comes to rank input parameters, the SA outcomes of experimental and theoretical DIs are consistent; see Fig. 9 (a). According to Eq. (12), DI_1 has a linear and monotonic relationship with the pump and carrier voltages. The V_p and V_c zones in Fig. 8 (a) also point to this type of relationship. Experimental results, however, demonstrate that DI_1 and carrier voltage have a quadratic relationship; see V_c^2 term in Fig. 7 (a). It is due to the electric/electronic nonlinearity that occurs when the carrier voltage is increased. This effect also contributes to the importance of V_c-related interaction terms in experimental outcomes, such as V_c: f_c. Because the measurement system's nonlinearity is weaker for low-frequency ranges,V_p^2 has a smaller impact on all DIs if it

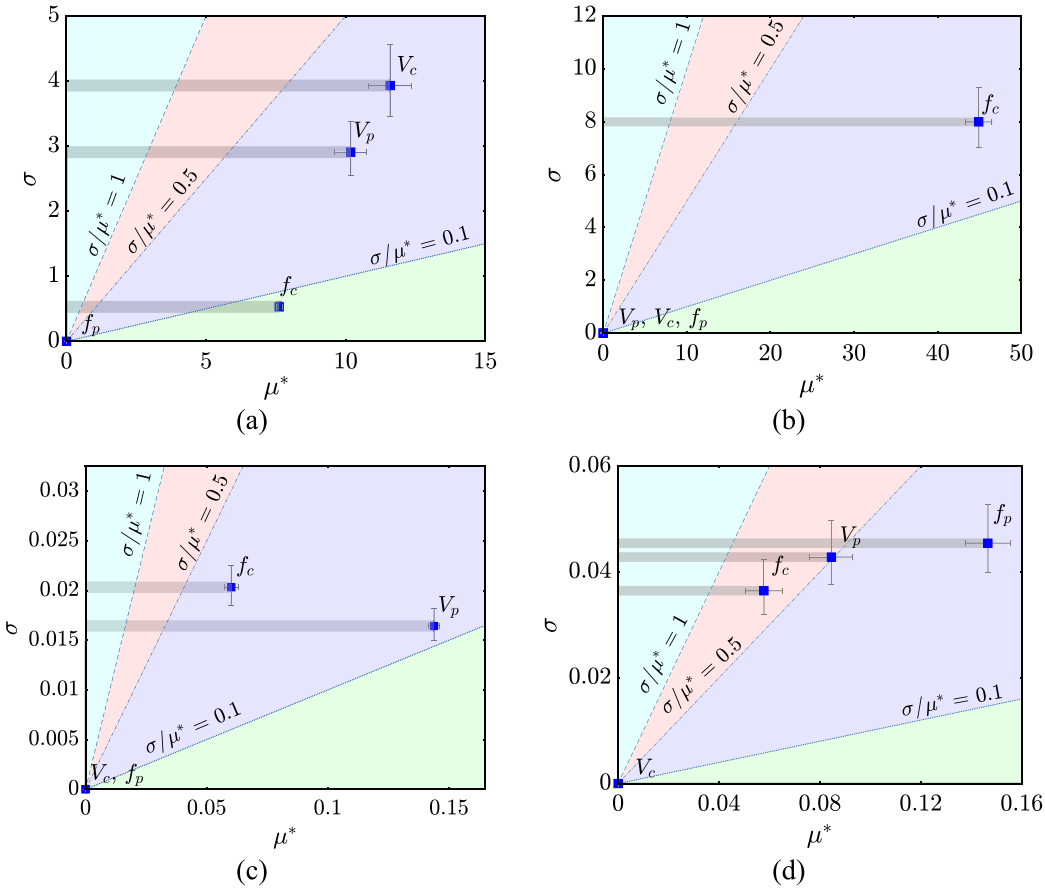

Fig. 8. Graphical representation of Morris sensitivity measures on σ-μ^* planes; (a) DI_1; (b) DI_2; (c) DI_3; (d) DI_4; the colors correspond to linear and additive; monotonic; nearly monotonic; nonlinear/non-monotonic relation between the control variables and the target DI.

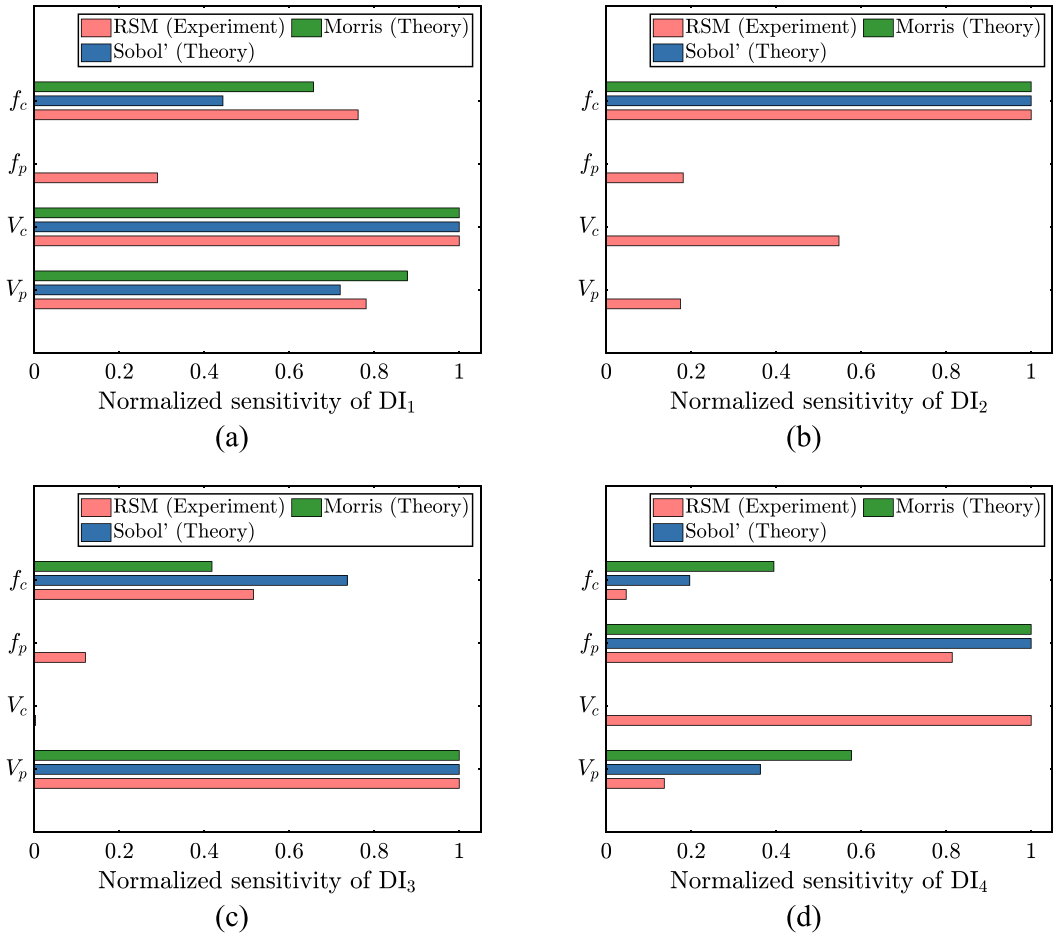

Fig. 9. Comparison of normalized sensitivity indices of the RSM, Morris and Sobol approaches; (a) DI_1; (b) DI_2; (c) DI_3; (d) DI_4.

exists. Except for CAN, all other sources of nonlinearity are ignored in the simplified SDOF model, including measurement system nonlinearities. Therefore, the relationship between the DI_1 and input voltages remains linear in Fig. 8 (a). This can be used to differentiate the CAN-induced nonlinearities from other sources, making the technique baseline-free.

In the case of DI_2, normalization to the pump and carrier excitation voltages leads to theoretical analysis independence from these parameters [6]; see Eq. (13) and Fig. 8 (b). In the experiment, however, DI_2 is still sensitive to a minimum value for the excitation voltage V_c. The reason is that the noise effect is taken into account while calculating the experimental DIs. More specifically, considering the noise level causes sidebands and hence damage to be undetectable for some combinations of input variables, especially when the input voltages are low, such as 10 V. Such input variables were penalized in response surface calculations. The noise effect, which is crucial in low-profile PZT-actuated VAM, is highlighted in this way. This adjustment makes the DIs sensitive to the lowest excitation voltages required to distinguish distinct sidebands from noise. This effect was negligible in this case study because the tests were conducted in a lab setting. Only two of the 81 tested cases had the sidebands buried in the noise level estimated with a safety factor of three. For in-situ tests in noisy environments, the effect can be much more substantial. Unlike V_c, the experimental results show no dependence on V_p. This is because the vibration amplitude of low-frequency pump modes is larger than the high-frequency carrier modes. Moreover, the test specimen is small, and a pump voltage of 10 V is sufficient to distinguish the damage from the noise level in the tests. In the case of large-scale components, the pump voltage must be high enough to detect damage. To summarize, the normalized DIs with respect to input voltages do not improve with the amplification of the actuation amplitudes. It could be a desirable feature that allows the amplifier to be removed from the setup or reduces high-voltage risks. When employing these DIs for damage detection in practice, however, it is important to make sure that the input voltages are high enough to distinguish between the sidebands and background noise and that the waves can withstand structural damping-induced attenuation.

In the case of DI_3, the theoretical and experimental results are completely consistent; see Fig. 9 (c). V_p has the greatest influence on DI_3, because its increase causes more periodic changes in contact pressure, which leads to more amplitude modulation. V_c has little effect on DI_3 as it can be deduced from the AM definition of Eq. (15), which is normalized by the carrier amplitude H_c. In terms of actuation frequency, DI_3 is predominantly influenced by the f_c and LDR effects. The f_p effect is only related to the modal effects, which are minimal in the experiments and non-existent in the theory.

The experimental and theoretical findings for DI_4 are comparable except for the carrier voltage; see Fig. 9 (d). V_c has the greatest impact on experimental outcomes, while theoretical outcomes show V_c independence. This is due to the total harmonic distortion that amplifiers apply to the actuation phases. Increasing the voltage, particularly in the high-frequency range, i.e., V_c, enhances FM significantly. It is an unfavorable consequence because it necessitates a baseline signal for reliable damage detection with DI_4. In comparison to other DIs, DI_4 has a different sensitivity for actuation frequency. DI_4 is more influenced by f_p than f_c due to the direct

inclusion of f_p in its definition. It results in DI_4 being influenced not only by the frequency response characteristics around the pump frequency but also by its absolute value.

5.2. Individual effects of control parameters on DIs

To further explore the primary effects of control parameters while removing interaction effects linked to non-damage-related nonlinearities, the first-order Sobol' index for the theoretical DI_1 and the adjusted main effect values for the experimental DI_1 were calculated and depicted in Fig. 10. The adjusted main effect of each control variable is calculated as the mean of the variation in the response, with all other predictors averaged out. The horizontal bars in Fig. 10 (a) locate the expected value of the adjusted response function as a measure of sensitivity. The horizontal lines in that figure show the confidence interval for the mean estimation. The normalized version of the sensitivity indices for each factor is shown in Fig. 10 (c). Although the results are for DI_1, a similar approach might be used for other DIs.

The importance of input voltages is introduced approximately identically in theory and experiment. The minor difference in theoretical results is due to the different ranges considered for V_p and V_c. When it comes to the input frequencies, however, there are some inconsistencies among the results. The carrier frequency is more important in the experiment than it is in the theory. This could be due to dissipative mechanisms and their accompanying thermal effects on the damaged contact surfaces, which are intensified by increased carrier frequency [19]. Increased carrier frequency enhances friction mechanisms between contacting mates, resulting in more energy being released as heat. Nonlinearity generated by thermal effects and time-dependent changes in geometry caused by a varying temperature field results in higher sidebands [34]. Although the roughness of the mating surfaces is taken into account indirectly in the theoretical analysis via C and n in the contact force (Eq. (1)), the simplified model ignores the dissipative and thermal effects of friction. Therefore, the carrier frequency's effect is estimated to be less in theory.

In the case of pump frequency, Fig. 10 (c) demonstrates that f_p is of minor importance in experiments, while the theory indicates independence from f_p. The former demonstrates that chosen acoustic modes for pump actuation have a similar potential for triggering nonlinear mechanisms. The SDOF model cannot include the modal effects of stimulations. Additionally, the frequency range commonly used for pump actuation is limited in VAM, and the structure's frequency response does not alter significantly in that range. As a result, the theoretical results indicate that DI_1 is approximately independent of f_p.

5.3. Direction of control parameter effects on DIs

Adjusting the input settings of VAM testing to the optimal value requires an understanding of the degree of sensitivity of the target DI to control parameters. The direction of control parameter effects further implies that the optimal setting can be attained by either decreasing or increasing the relevant parameter. The correlation sign of the target DI and the control parameters can be inferred from the sign of the μ measure in Morris results. For DI_1, for example, Fig. 11 (a) shows the μ measure of the control settings in the

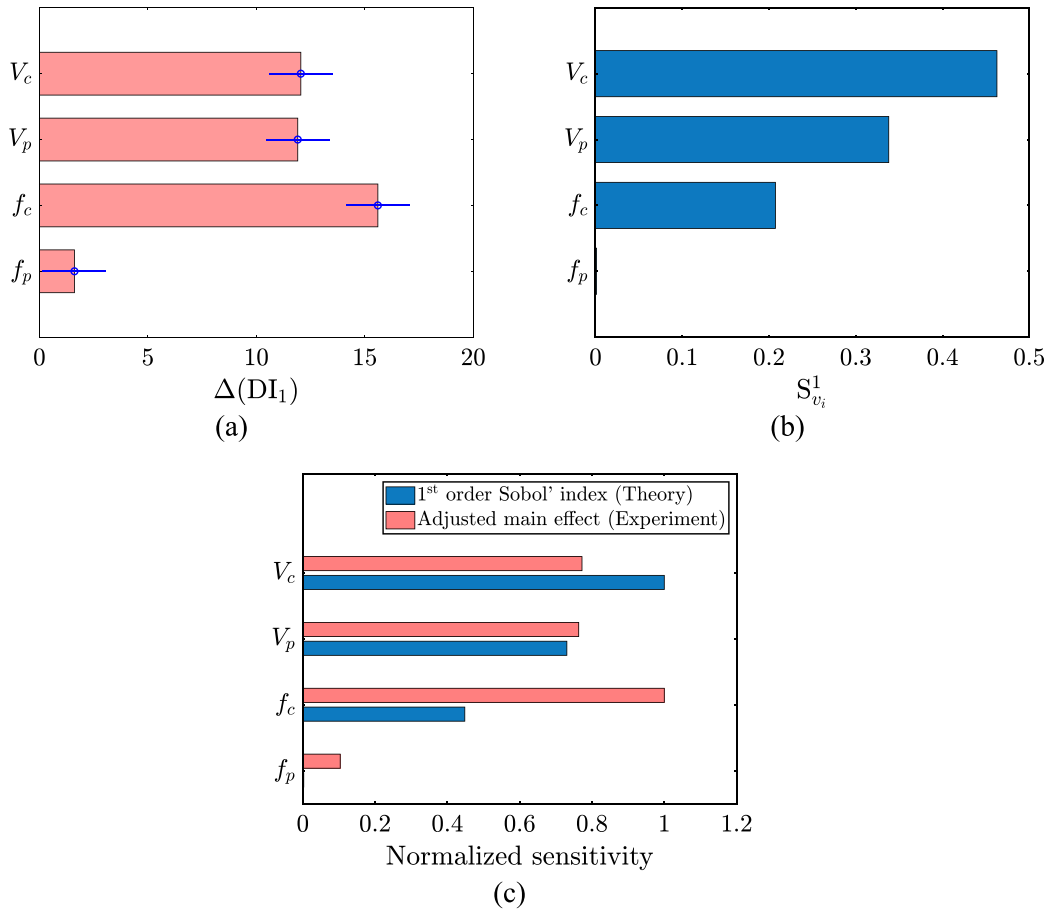

Fig. 10. The individual effects of the control parameters on DI_1: (a) adjusted main effects on the experimental DI_1 (b) 1st order Sobol' indices for the theoretical DI_1 (c) normalized individual effects on DI_1.

σ-μ plane. μ is positive for input voltages, negative for the carrier frequency, and nearly zero but positive for the pump frequency. Hence, increasing the input voltages while decreasing the carrier frequency is theoretically advantageous. The latter is owing to the frequency response characteristic that as the frequency is moved away from the natural frequency, the response amplitude decreases. Because the SDOF model's only natural frequency is chosen between the pump and carrier frequencies, μ is positive for f_p and negative for f_c. The variation range for pump frequency in VAM experiments is narrow, hence μ is a low number for f_p. The results emphasize that shifting the input frequencies toward the frequency response peak values enhances the VAM's ability to identify damage. This is especially important when the frequency response partially shifts as the damage progresses.

In the case of experimental results, a normal probability plot of standardized effects can be used to identify the direction of the control factors' influence on the target DI. The standardized effects (t-value) for DI_1 are depicted in Fig. 11(b) with respect to a normal fit line, which represents the case when all effects are zero. The factors on the right (or left) of the fit line imply a positive (or negative) impact on the target DI. The factors closer to the fit line are less influential, as is the case for the interaction terms. The factors labeled as insignificant do not statistically affect DI_1. For pump frequency, the sign of effect in the experimental findings agrees with the theory. The dependence on f_p in the experiments is related to the modal effects, which are positive in this case study, showing that the 475 Hz mode is slightly better than the other two, but not significantly. The signs of input voltage impacts on DI_1 are also positive, as predicted by theory, indicating that increasing the input voltages increases the detectability of damage. The estimated sign of the effect in the case of carrier frequency, however, is inconsistent in theory and experiment. This is true not only for DI_1, but for all other DIs as well. It is mostly linked to the more effective interaction of the higher-frequency carrier wave with the damage to trigger the nonlinear mechanisms stated in Section 5.2. It is also linked to the structural damping effect, which causes the frequency response of high-frequency regimes to be nearly identical in amplitude. Hence, the frequency response effect, which is the only influence reflected in the theoretical analysis, is ignorable in practice. The LDR influence of the carrier frequency, on the other hand, is significant in practice. In conclusion, increasing the pump and carrier excitation voltages, as well as the carrier frequency improves DI_1's ability to detect or image damage using the VAM technique. The pump frequency must be chosen optimally using the procedure described in Section 4.1. The reported results can be used to derive similar guidelines for other DIs.

6. Conclusion

The sensitivity of VAM damage measurements for pump and carrier voltages and frequencies was explored to optimize control settings in VAM testing. The discrete influence of the structure's frequency response on the formation of the sidebands was addressed using RSM with input frequencies as discrete variables. To determine the response surface, 81 experiments were designed using CCD. The experiments were performed on a sandwich beam with contact nonlinearity caused by bolt loosening. Spectral and demodulation DIs were derived analytically for an SDOF model considering PZT actuation effects. Sample-based SA was also performed on analytical DIs, and the results were compared to experiments. The key findings are as follows:

- The type of DI used to diagnose the defect determines its sensitivity to or independence from control parameters.
- The dependence of spectral DIs on input voltages is theoretically linear. However, nonlinearities that are not caused by damage, such as those induced by the measurement system, yield quadratic or higher-order effects. Measurement system-induced nonlinearities have a significant impact on DI levels, particularly FM.
- The normalized DIs with respect to input voltages do not further increase with actuation amplitude amplification if the input voltages are adequate to identify the sidebands from the noise level and the waves can withstand attenuation due to structural damping.
- Pump frequency affects damage detectability primarily through its modal effects. The exception is FM-derived DI, which is also affected by the pump frequency value.
- Increasing the carrier frequency enhances the wave-damage interaction and damage-induced nonlinearity, which is advantageous for damage identification with all DIs.

The findings of this study can be used as inputs to an optimization program for selecting appropriate DIs and fine-tuning the adjustable parameters to maximize the damage detectability via the targeted DI in the VAM technique. Although the SDOF model

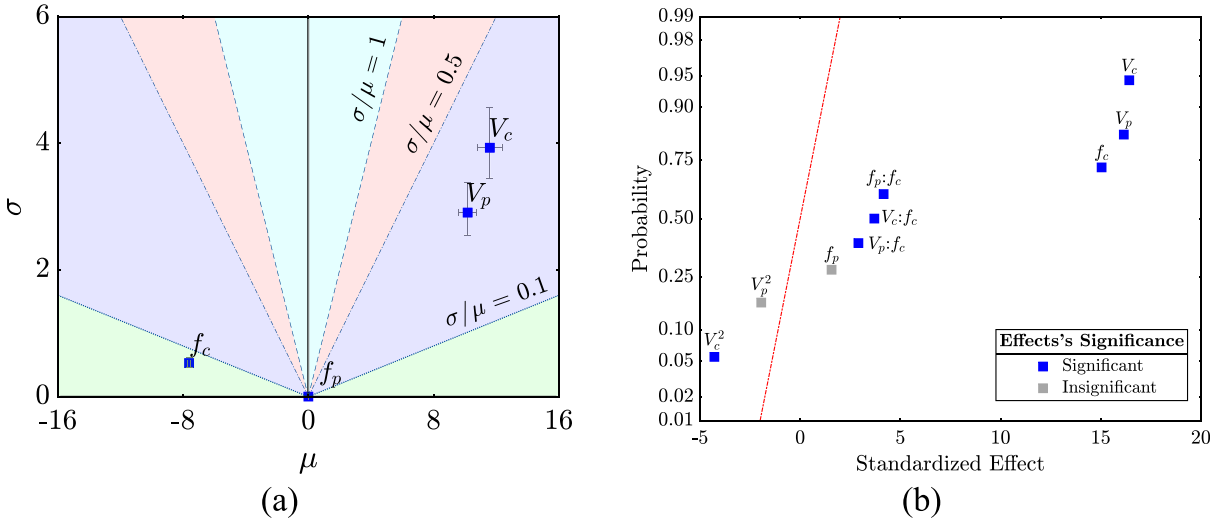

Fig. 11. The sensitivity sign of DI_1 for the control parameters: (a) Morris sensitivity measures μ in the σ-μ plane (b) Normal probability plot for standardized effects of control settings.

reflects the fundamental principles of contact-induced intermodulation rather well, there are some discrepancies between the model's predictions and experiments due to the simplifying assumptions used in its development. Hence, future investigations should use more detailed numerical models of VAM in the proposed framework [64].

Funding

This research received no specific grant from any funding agency in the public, commercial, or not-for-profit sectors.

CRediT authorship contribution statement

Mohammad Ehsani: Conceptualization, Methodology, Software, Visualization, Data curation, Formal analysis, Investigation, Validation, Writing – original draft, Writing – review & editing. **Mahnaz Shamshirsaz:** Conceptualization, Supervision, Project administration, Writing - review & editing. **Mojtaba Sadighi**: Conceptualization, Supervision, Writing – review & editing. **Naserodin Sepehry:** Visualization, Conceptualization, Data curation, Methodology, Writing – review & editing. **Richard Loendersloot**: Conceptualization, Data curation, Methodology, Writing review & editing.

Declaration of Competing Interest

The authors declare that they have no known competing financial interests or personal relationships that could have appeared to influence the work reported in this paper.

Data availability

No data was used for the research described in the article.

Appendix

Appendix A. Amplitudes of harmonics in the response of the SDOF system with contact nonlinearity to a biharmonic excitation

The amplitudes of spectral components in equation (11) are read:

$$H_p = \frac{A_p}{\omega_0^2 - \omega_p^2};\ H_c = \frac{A_c}{\omega_0^2 - \omega_c^2} \tag{A.1}$$

$$G_{hp} = -\frac{\varepsilon k_2 A_p^2}{2m\left(\omega_0^2 - 4\omega_p^2\right)\left(\omega_0^2 - \omega_p^2\right)^2};$$
$$G_{hc} = -\frac{\varepsilon k_2 A_c^2}{2m(\omega_0^2 - 4\omega_c^2)(\omega_0^2 - \omega_c^2)^2} \tag{A.2}$$

$$G_{sb^-} = -\frac{\varepsilon k_2 A_c A_p}{m(\omega_0^2 - \omega_c^2)\left(\omega_0^2 - \omega_p^2\right)\left(\omega_0^2 - (\omega_c - \omega_p)^2\right)} \tag{A.3}$$

$$G_{sb^+} = -\frac{\varepsilon k_2 A_c A_p}{m(\omega_0^2 - \omega_c^2)\left(\omega_0^2 - \omega_p^2\right)\left(\omega_0^2 - (\omega_c + \omega_p)^2\right)} \tag{A.4}$$

Appendix B. Demodulation DIs considering zero phase angles for actuation signals

Assuming zero phase actuation signals that result in zero phase sensor spectral components for the proposed CAN model, the instantaneous amplitude can be determined as follows using Eq. (14):

$$A_{ins}(t) = \left|H_c + (G_{sb^+} + G_{sb^-})\cos(\omega_p t) + i(G_{sb^+} - G_{sb^-})\sin(\omega_p t)\right| \tag{B.1}$$

To determine $A_{ins_{PP}}$, the maximum and minimum values of the instantaneous amplitude over the duration of signal sampling T are calculated as follows:

$$\max_{t\in T}(\min)\{|A_{ins}(t)|\} = \sqrt{\max_{t\in T}(\min)\left\{|A_{ins}(t)|^2\right\}} = \sqrt{\max_{t\in T}(\min)\left\{\underbrace{\begin{array}{c}H_c^2 + (G_{sb^+} + G_{sb^-})^2\cos^2(\omega_p t) + 2H_c(G_{sb^+} + G_{sb^-})\cos(\omega_p t)\\ +(G_{sb^+} - G_{sb^-})^2\sin^2(\omega_p t)\end{array}}_{e(t)}\right\}} \tag{B.2}$$

The derivative of $e(t)$ is set to zero to find the extrema, yielding two sets of solutions:

$$\sin(\omega_p t) = 0 \rightarrow t = m\pi/\omega_p;\ m = 0, 1, \ldots \tag{B.3}$$

$$\cos(\omega_p t) = \frac{H_c(G_{sb^+} + G_{sb^-})}{(G_{sb^+} - G_{sb^-})^2 - (G_{sb^+} + G_{sb^-})^2} = \frac{-H_c(G_{sb^+} + G_{sb^-})}{4G_{sb^+}G_{sb^-}} \tag{B.4}$$

Eq. (B.4) holds only if the right-hand side of the equation is between −1 and 1. However, the numerator is greater than the denominator because the carrier amplitude (H_c) is significantly greater than the modulation amplitudes (G_{sb^+} and G_{sb^-}), preventing such extrema. Therefore, Eq. (B.3) is used to calculate the peak-to-peak value of instantaneous amplitude as follows:

$$A_{ins_{pp}} = \max_{t\in T}\{A_{ins}(t)\} - \min_{t\in T}\{A_{ins}(t)\} = |H_c + (G_{sb^+} + G_{sb^-})| - |H_c - (G_{sb^+} + G_{sb^-})| = 2(G_{sb^+} + G_{sb^-}) \tag{B.5}$$

$H_c \gg (G_{sb^+} + G_{sb^-})$ has been used to identify the sign of expressions inside the absolute value in the above equation. Using Eq. (15) and Eq. (B.5), the AM intensity is obtained as follows:

$$DI_3 = (G_{sb^+} + G_{sb^-})/H_c \tag{B.6}$$

By substituting the spectral amplitudes from Eq. (A.1) and Eqs. (A.3) and (A.4), Eq. (17) is obtained.

To derive DI_4 associated with FM, the instantaneous phase is determined as follows, assuming zero-phase for sensor components:

$$\varphi_{ins}(t) = \measuredangle \delta_a(t) = \omega_c t + \arctan\left(\frac{(G_{sb^+} - G_{sb^-})\sin(\omega_p t)}{H_c + (G_{sb^+} + G_{sb^-})\cos(\omega_p t)}\right) \quad (B.7)$$

The instantaneous frequency is the time-derivative of the instantaneous phase:

$$\omega_{ins}(t) = \omega_c + \frac{(G_{sb^-} - G_{sb^+})\omega_p(G_{sb^-} + G_{sb^+} + H_c\cos(\omega_p t))}{G_{sb^-}^2 + 2H_c(G_{sb^-} + G_{sb^+})\cos(\omega_p t) + 2G_{sb^-}G_{sb^+}\cos(2\omega_p t) + G_{sb^+}^2 + H_c^2} \quad (B.8)$$

By substituting ω_{ins} into Eq. (16), we get:

$$DI_4 = \max\left\{\left|\frac{(G_{sb^-} - G_{sb^+})(G_{sb^-} + G_{sb^+} + H_c\cos(\omega_p t))}{G_{sb^-}^2 + 2H_c(G_{sb^-} + G_{sb^+})\cos(\omega_p t) + 2G_{sb^-}G_{sb^+}\cos(2\omega_p t) + G_{sb^+}^2 + H_c^2}\right|\right\} \quad (B.9)$$

By equating the derivative of the above expression to zero, the maximum values are found at $t = m\pi/\omega_p$ where $m = 0, 1, \ldots$. As a result, the analytical expression for DI_4 is as follows:

$$DI_4 = \frac{(G_{sb^-} - G_{sb^+})(G_{sb^-} + G_{sb^+} + H_c)}{G_{sb^-}^2 + 2H_c(G_{sb^-} + G_{sb^+}) + 2G_{sb^-}G_{sb^+} + G_{sb^+}^2 + H_c^2} = \frac{G_{sb^-} - G_{sb^+}}{G_{sb^-} + G_{sb^+} + H_c} \quad (B.10)$$

which yields the explicit form of Eq. (18) by replacing H_c, G_{sb^-} and G_{sb^+} from Eq. (A.1) and Eqs. (A.3) and (A.4).

Appendix C. Supplementary data

Supplementary data to this article can be found online at https://doi.org/10.1016/j.apacoust.2022.109193.

References

[1] Birman V, Kardomateas GA. Review of current trends in research and applications of sandwich structures. Compos B Eng 2018;142:221–40.
[2] Zhao N, Huo L, Song G. A nonlinear ultrasonic method for real-time bolt looseness monitoring using PZT transducer–enabled vibro-acoustic modulation. J Intell Mater Syst Struct 2020;31(3):364–76.
[3] Masmoudi S, El Mahi A, Turki S. Fatigue behaviour and structural health monitoring by acoustic emission of E-glass / epoxy laminates with piezoelectric implant. Appl Acoust 2016;108:50–8.
[4] Wang F, Song G. Monitoring of multi-bolt connection looseness using a novel vibro-acoustic method. Nonlinear Dyn 2020;100(1):243–54.
[5] Wang F, Song G. Bolt early looseness monitoring using modified vibro-acoustic modulation by time-reversal. Mech Syst Signal Process 2019;130:349–60.
[6] Zhang Z, Xiao Y, Xie Y, Su Z. Contact acoustic nonlinearity (CAN)-based continuous monitoring of bolt loosening: Hybrid use of high-order harmonics and spectral sidebands. Compos Struct 2019;211:13–23.
[7] Zhang Z, Liu M, Su Z, Xiao Y. Quantitative evaluation of residual torque of a loose bolt based on wave energy dissipation and vibro-acoustic modulation: A comparative study. J Sound Vib 2016;383:156–70.
[8] He Y, Xiao Y, Su Z, Pan Y, Zhang Z. Contact acoustic nonlinearity effect on the vibro-acoustic modulation of delaminated composite structures. Mech Syst Signal Process 2022;163:108161.
[9] Yoder NC, Adams DE. Vibro-acoustic modulation utilizing a swept probing signal for robust crack detection. Struct Heal Monit 2010;9(3):257–67.
[10] Amerini F, Meo M. Structural health monitoring of bolted joints using linear and nonlinear acoustic/ultrasound methods. Struct Heal Monit 2011;10(6):659–72.
[11] Chrysochoidis NA, Assimakopoulou TT, Saravanos DA. Nonlinear wave structural health monitoring method using an active nonlinear piezoceramic sensor for matrix cracking detection in composites. J Intell Mater Syst Struct 2015;26(15):2108–20.
[12] Zagrai A, Donskoy D, Chudnovsky A, Golovin E. Micro-and macroscale damage detection using the nonlinear acoustic vibro-modulation technique. Res Nondestruct Eval 2008;19(2):104–28.
[13] Chen J, Wu Y, Yang C. Damage assessment of concrete using a non-contact nonlinear wave modulation technique. NDT E Int 2019;106(May):1–9.
[14] Klepka A, Pieczonka L, Staszewski WJ, Aymerich F. Impact damage detection in laminated composites by non-linear vibro-acoustic wave modulations. Compos Part B Eng 2014;65:99–108.
[15] Chen BY, Soh SK, Lee HP, Tay TE, Tan VBC. A vibro-acoustic modulation method for the detection of delamination and kissing bond in composites. J Compos Mater 2016;50(22):3089–104.
[16] Singh AK, Chen B, Tan VBC, Tay TE, Lee HP. A theoretical and numerical study on the mechanics of vibro-acoustic modulation. J Acoust Soc Am 2017;141(4):2821–31.
[17] Wei L, Chen J. Experimental and numerical characterization of delamination features in orthotropic CFRP laminates using pre-modulated waves. Appl Acoust 2022;201:109102.
[18] Pieczonka L, Ukowski P, Klepka A, Staszewski WJ, Uhl T, Aymerich F. Impact damage detection in light composite sandwich panels using piezo-based nonlinear vibro-acoustic modulations. Smart Mater Struct 2014;23(10):pp.
[19] Klepka A, Staszewski WJ, Jenal RB, Szwedo M, Iwaniec J, Uhl T. Nonlinear acoustics for fatigue crack detection - experimental investigations of vibro-acoustic wave modulations. Struct Heal Monit 2012;11(2):197–211.
[20] Van Den Abeele K-A, Johnson PA, Sutin A. Nonlinear elastic wave spectroscopy (NEWS) techniques to discern material damage, part I: nonlinear wave modulation spectroscopy (NWMS). J Res Nondestruct Eval 2000;12(1):17–30.
[21] Liu B, Yang J, Zhang G, Gang T. The choice of the sweep-frequency rate for the probing wave in nonlinear-modulation method of crack detection in resonant samples. NDT E Int 2021;123:102524.
[22] Guyer RA, McCall KR, Van Den Abeele K. Slow elastic dynamics in a resonant bar of rock. Geophys Res Lett 1998;25(10):1585–8.
[23] Zaitsev VY, Gusev V, Castagnede B. Observation of the 'Luxemburg–Gorky effect' for elastic waves. Ultrasonics 2002;40(1–8):627–31.
[24] Donskoy D, Sutin A, Ekimov A. Nonlinear acoustic interaction on contact interfaces and its use for nondestructive testing. Ndt E Int 2001;34(4):231–8.
[25] Li N, Sun J, Jiao J, Wu B, He C. Quantitative evaluation of micro-cracks using nonlinear ultrasonic modulation method. NDT E Int 2016;79:63–72.
[26] Duffour P, Morbidini M, Cawley P. Comparison between a type of vibro-acoustic modulation and damping measurement as NDT techniques. NDT E Int 2006;39(2):123–31.
[27] Klepka A, Staszewski WJ, Di Maio D, Scarpa F. Impact damage detection in composite chiral sandwich panels using nonlinear vibro-acoustic modulations. Smart Mater Struct 2013;22(8):84011.
[28] R. Wang, J. Li, S. An, H. Hao, W. Liu, and L. Li, "Densely connected convolutional networks for vibration based structural damage identification," *Eng. Struct.*, vol. 245, no. October 2020, p. 112871, 2021.
[29] Liu P, Sohn H. Damage detection using sideband peak count in spectral correlation domain. J Sound Vib 2017;411:20–33.
[30] X. Qin *et al.*, "Full life-cycle monitoring and earlier warning for bolt joint loosening using modified vibro-acoustic modulation," *Mech. Syst. Signal Process.*, vol. 162, no. May 2021, p. 108054, 2022.
[31] Oppermann P, Dorendorf L, Rutner M, Renner C. Nonlinear modulation with low-power sensor networks using undersampling. Struct Heal Monit 2021;20(6):3252–64.
[32] Ooijevaar T, Rogge MD, Loendersloot R, Warnet L, Akkerman R, Tinga T. Vibro-acoustic modulation–based damage identification in a composite skin–stiffener structure. Struct Heal Monit 2016;15(4):458–72.
[33] H. F. Hu, W. J. Staszewski, N. Q. Hu, R. B. Jenal, and G. J. Qin, "Crack detection using nonlinear acoustics and piezoceramic transducers-instantaneous amplitude and frequency analysis," *Smart Mater. Struct.*, vol. 19, no. 6, 2010.
[34] Dziedziech K, Klepka A, Roemer J, Pieczonka L. Experimental study of thermo-acoustic wave modulation in a cracked plate. J Sound Vib 2021;498:1–16.
[35] Lim HJ, Sohn H, Desimio MP, Brown K. Reference-free fatigue crack detection using nonlinear ultrasonic modulation under various temperature and loading conditions. Mech Syst Signal Process 2014;45(2):468–78.
[36] Klepka A, Dziedziech K, Mrówka J, Górski J. Experimental investigation of modulation effects for contact-type interfaces in vibro-acoustic modulation tests. Struct Heal Monit 2021;20(3):917–30.
[37] Houhat N, Tournat V, Ménigot S, Boutkedjirt T, Girault JM. Optimal pump excitation frequency for improvement of damage detection by nonlinear vibro acoustic modulation method in a multiple scattering sample. Appl Acoust 2019;155:222–31.
[38] Pieczonka L, Zietek L, Klepka A, Staszewski WJ, Aymerich F, Uhl T. Damage imaging in composites using nonlinear vibro-acoustic wave modulations. Struct Control Heal Monit 2018;25(2):1–13.
[39] Solodov I, Bai J, Bekgulyan S, Busse G. A local defect resonance to enhance acoustic wave-defect interaction in ultrasonic nondestructive evaluation. Appl Phys Lett 2011;99(21):3–6.
[40] D. Dionysopoulos, G. P. M. Fierro, M. Meo, and F. Ciampa, "Imaging of barely visible impact damage on a composite panel using nonlinear wave modulation thermography," *NDT E Int.*, vol. 95, no. July 2017, pp. 9–16, 2018.
[41] Joglekar DM. Analysis of nonlinear frequency mixing in Timoshenko beams with a breathing crack using wavelet spectral finite element method. J Sound Vib 2020;488:115532.
[42] Donskoy D, Liu D. Vibro-acoustic modulation baseline-free non-destructive testing. J Sound Vib 2021;492:115808.
[43] Zhang C, He L, Liu S, Yang Q. A new vibro-acoustic modulation technique for closed crack detection based on electromagnetic loading. Appl Acoust 2020;157:107004.
[44] Delrue S, Van Den Abeele K. Three-dimensional finite element simulation of closed delaminations in composite materials. Ultrasonics 2012;52(2):315–24.
[45] Zaitsev VY, Matveev LA, Matveyev AL. On the ultimate sensitivity of nonlinear-modulation method of crack detection. NDT E Int 2009;42(7):622–9.
[46] Prawin J, Rama Mohan Rao A. Vibration-based breathing crack identification using non-linear intermodulation components under noisy environment. Struct Heal Monit 2020;19(1):86–104.

[47] Lim HJ et al. Development and field application of a nonlinear ultrasonic modulation technique for fatigue crack detection without reference data from an intact condition. Smart Mater Struct 2016;25(9):1–14.
[48] Biwa S, Nakajima S, Ohno N. On the acoustic nonlinearity of solid-solid contact with pressure-dependent interface stiffness. J Appl Mech Trans ASME 2004;71 (4):508–15.
[49] Li N, Wang F, Song G. Monitoring of bolt looseness using piezoelectric transducers: Three-dimensional numerical modeling with experimental verification. J Intell Mater Syst Struct Feb. 2020;31(6):911–8.
[50] Baltazar A, Rokhlin SI, Pecorari C. On the relationship between ultrasonic and micromechanical properties of contacting rough surfaces. J Mech Phys Solids 2002;50(7):1397–416.
[51] Xiao H, Shao Y, Brennan MJ. On the contact stiffness and nonlinear vibration of an elastic body with a rough surface in contact with a rigid flat surface. Eur J Mech A/Solids 2015;49:321–8.
[52] Croccolo D, De Agostinis M, Vincenzi N. Failure analysis of bolted joints: Effect of friction coefficients in torque-preloading relationship. Eng Fail Anal 2011;18 (1):364–73.
[53] Giurgiutiu V. Tuned Lamb wave excitation and detection with piezoelectric wafer active sensors for structural health monitoring. J Intell Mater Syst Struct 2005;16(4):291–305.
[54] Donskoy DM, Ramezani M. Separation of amplitude and frequency modulations in Vibro-Acoustic Modulation nondestructive testing method. Proc. Meet. Acoust. 2018;34(1).
[55] Weisberg S. Applied linear regression. John Wiley & Sons; 2013.
[56] Park S, Lee C, Sohn H. Reference-free crack detection using transfer impedances. J Sound Vib 2010;329(12):2337–48.
[57] Wang Y, Qin X, Huang S, Lu L, Zhang Q, Feng J. Structural-borne acoustics analysis and multi-objective optimization by using panel acoustic participation and response surface methodology. Appl Acoust 2017;116:139–51.
[58] Campolongo F, Cariboni J, Saltelli A. An effective screening design for sensitivity analysis of large models. Environ Model Softw 2007;22 (10):1509–18.
[59] Morris MD. Factorial sampling plans for preliminary computational experiments. Technometrics 1991;33(2):161–74.
[60] Sanchez DG, Lacarrière B, Musy M, Bourges B. Application of sensitivity analysis in building energy simulations : Combining first- and second-order elementary effects methods. Energy Build 2014;68:741–50.
[61] Bhalla S, Gupta A, Bansal S, Garg T. Ultra low-cost adaptations of electro-mechanical impedance technique for structural health monitoring. J Intell Mater Syst Struct 2009;20(8):991–9.
[62] Parsons Z, Staszewski WJ. Nonlinear acoustics with low-profile piezoceramic excitation for crack detection in metallic structures. Smart Mater Struct 2006;15(4):1110–8.
[63] Aumond P, Can A, Mallet V, Gauvreau B, Guillaume G. Global sensitivity analysis for road traffic noise modelling. Appl Acoust 2021;176:107899.
[64] N. Sepehry, M. Ehsani, W. Zhu, and F. Bakhtiari-Nejad, "Application of scaled boundary finite element method for vibration-based structural health monitoring of breathing cracks," J. Vib. Control, p. 1077546320968646, 2020.